A coupled PIC-Poisson-solver code for the extraction of charged particles from a negative ion source

F. Sattin[1#], A. Tanga[2], M. Cavenago[3], V. Antoni[1,4]

[1] *Consorzio RFX,Associazione Euratom-ENEA per la fusione,*

Corso Stati Uniti 4, 35127 Padova, Italy

[2] *Max-Planck-Institut für PlasmaPhysik,*

Boltzmannstrasse 2, 85748 Garching, Germany

[3] *INFN-LNL, viale dell'Università, 35020 Legnaro (PD), Italy*

[4]*INFM, Unità di Padova*

Abstract

Negative ion sources have since long been proposed as suitable production means of fast particle beams to be used in International Thermonuclear Experiment Reactor (ITER) as additional heating mechanisms. The numerical simulation of the particle production and extraction mechanisms within these sources is a valuable tool towards their optimisation. A challenging aspect of the problem of producing a realistic consistent model for the external applied fields, extracted particles and plasma boundary has been the large difference between the microscopic characteristic Debye length and the macroscopic size of the actual geometry. Therefore, a lot of work has been focussed on describing the extraction region over distances of the order of Debye sheath length. As a consequence, any macroscopical description-aimed at describing details over spatial scales of order of 10^{-2} m and larger-cannot be obtained within the same models by using realistic computer resources. Here, instead, a numerical code has been developed ex-novo by decoupling the problem: the model has been reduced to one of electrostatics coupled self-consistently to plasma dynamics, in which electric fields are both applied from the outside as well as partly generated by the motion of the charged particles. Non-trivial boundary conditions are to be supplemented, in order to describe the complicated geometry of the actual

[#] Corresponding author. Email: fabio.sattin@igi.cnr.it

sources. A realistic geometry has been used, attempting to model with quite detail the extraction geometry of the sources under development for the ITER injector. This geometry includes values of electrical and magnetic fields foreseen for the ITER injector. The code is designed to work in cases where the plasma density acts as a perturbation over the potential profiles or, equivalently, in the approximation of very strong applied extracting potentials compared to the plasma potential. In this work the present stage of development of such a numerical code is presented. Present results include: an assessment of the relative effectiveness of surface production versus volume production for extracting negative ions; and a study of the effectiveness of a magnetic filter in confining electrons away from the extraction region.

1. Introduction

Neutral beams from negative ion sources are expected to be one of the heating techniques chosen for ITER. The numerical simulation of the production and extraction mechanisms of negative hydrogen ions, hence, is necessary for the optimization of the source efficiency and as basis for the ion optics. However, consistent, physically correct and accurate simulations are plagued by difficulties. Numerically, the problem is that of solving the equations of motion for a large set of charged particles of several species moving within an electric field that is partially imposed by the outside (extraction potential) and partially generated by the charges themselves. All supplemented by non-trivial boundary conditions.

The subject has already been tackled in several works. Very often, the extraction region is virtually identified with the sheath or pre-sheath region [1-5]. Sheath region is, of course, highly relevant in connection with ion surface production, and may effectively coincide with the whole extraction region for very low-density plasmas. In sources designed to deliver high-intensity beams, however, the Debye length shrinks to such a small value that the sheath region is, to all purposes, invisible to investigation: the dynamics of the extraction occurs over spatial lengths much larger than that. This is due both to high density and to large extraction potentials. To give an estimate, in BATMAN source, the electron Debye length is $\lambda_D \approx 10^{-5}$ m (plasma parameters are taken from fig. 3 of ref. [6]). At the same time, length scales thought to be relevant for extraction (e.g., extraction holes' diameters, distances between electrodes, …) are of order several mm's. BATMAN-like sources are, presently, the main candidates as future NBI sources in ITER. A sketch of them is given in Fig. (1). The region of interest for this work is the one around the grids: there are three of them, named Plasma Grid, Extraction Grid, Acceleration Grid along the direction from the plasma to the outside. They are separated by a few mm's (Plasma Grid and Extraction Grid are so close together that in the figure cannot be clearly distinguished), and among them extraction potentials of some kV may be applied. Particles are extracted through holes of about 1 cm of diameter.

In order to satisfactorily model these sources, it is necessary, hence, at least to adapt existing algorithms. In the following, it will be described such a code, patterned after the work [5]: it is a Particle-In-Cell module for plasma dynamics coupled to a Poisson Equation solver for potential profile.

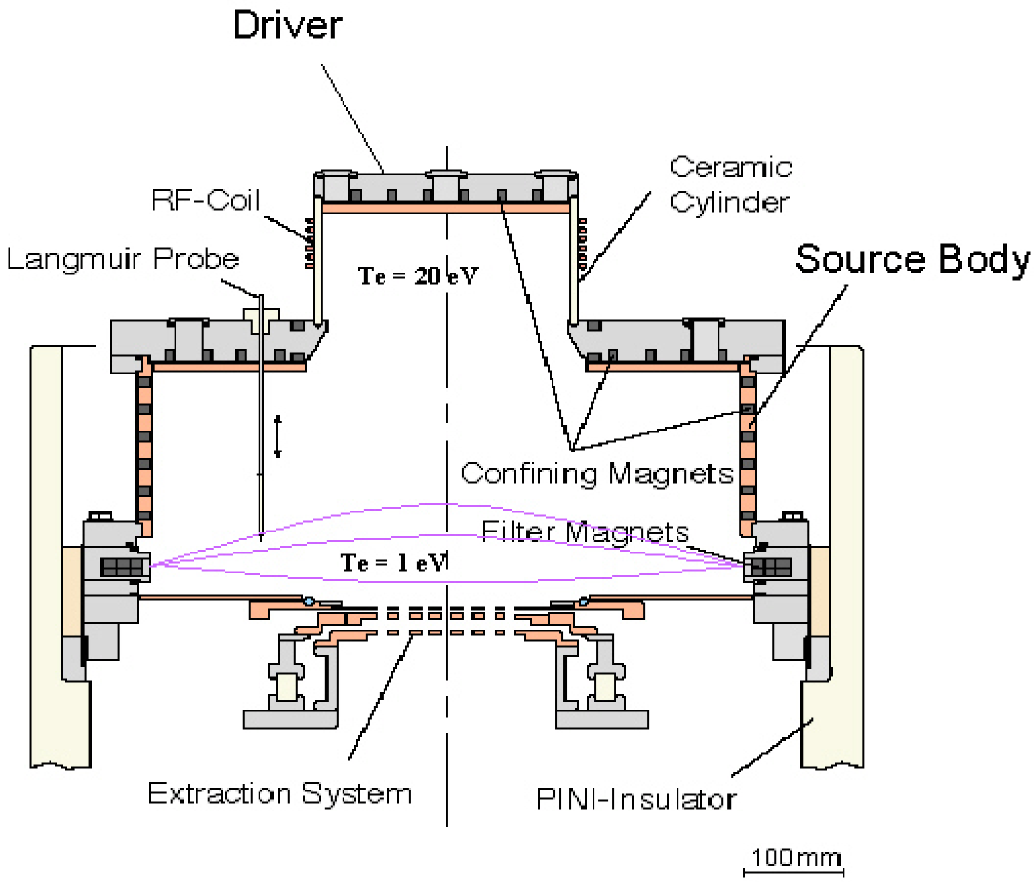

FIG. 1. Schematic view of negative source.

One concern with these codes is that the problem has intrinsically a large number of degrees of freedom, in the form of parameters that must be fed into the code from the outside, and that can often be known only poorly and/or partially through experiment [4]. Any attempt of developing a comprehensive code from scratch, therefore, can hardly be successful. Instead, it is more convenient to start from a very simplified model-both its geometry as well as the treatment of the particles inside-but still able to describe at least the gross features of the extraction process.

2. The numerical algorithm

An enlarged view of the basic 2-dimensional unit cell composing the grid is considered in Fig. (2). Uniformity is assumed along the third direction. (Holes in the grid, actually, do have circular shape). One must imagine a periodic array of these basic cells extending along *x*-axis.

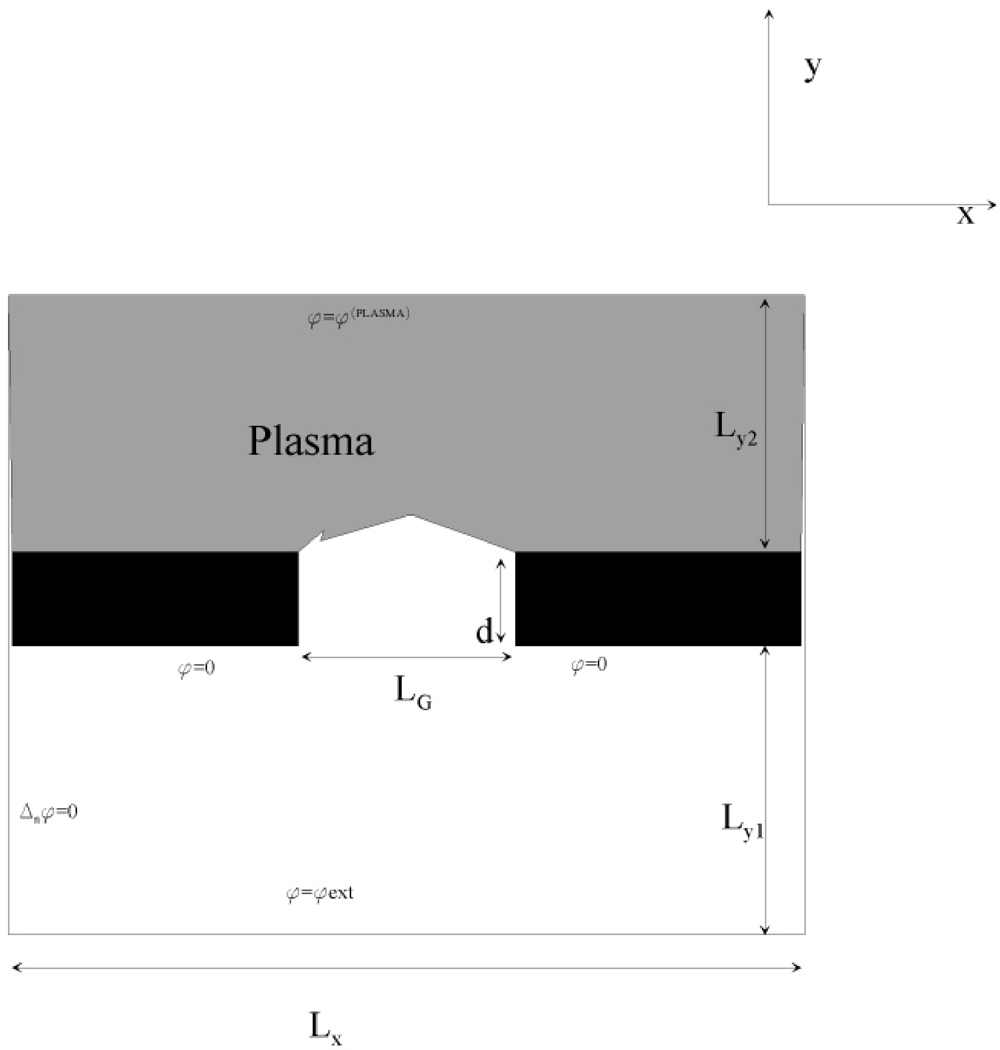

FIG. 2. Basic cell for computations. The black rectangles stand for the Plasma Grid, with the Extraction Hole in between. Above them, there is the confined plasma, and below the Extraction Region. The floor of the figure stands for the Extraction Grid; the ceiling for the "plasma boundary" (whose precise meaning is to be better explained later). The geometric sizes L_x (width of the cell), L_G (diameter of the hole), d (thickness of the Plasma Grid), L_{y1} (distance between Plasma Grid and Extraction Grid) are all geometric parameters known in advance of the computation. L_{y2}, instead, will be determined later.

A simplified model for plasma dynamics will be considered, neglecting particle-particle collisions (including ionization and recombination). Also particle-surface collisions will just lead to absorption of the particle: no reflection is permitted. A confining magnetic field (magnetic filter) is explicitly included: indeed, part of the simulations will address the issue of the performances of this field over particle confinement. Actual magnetic filters have a complicated pattern (see Fig. 1), however, the present stage of refinement of the code makes pointless the detailed simulation of the magnetic geometry, and we just limit to a constant magnitude field, directed along *z*-axis (i.e., perpendicular to the plane in figure).

Finally, three-components-plasmas will be considered: electrons, protons, and negative Hydrogen ions. The presence of doping elements, such as Caesium atoms, is deemed to act as a surface coating, without playing any active role in plasma dynamics.

The calculation performs iteratively, solving the Poisson equation at each iteration *k*

$$\nabla^2 \varphi^{(k)} = -\frac{e}{\varepsilon_0}\delta n^{(k-1)} \ , \quad k > 0 \qquad (1)$$

where $e\,\delta n = e\,(n_p - n_e - n_i)$ is the local charge density imbalance between electrons (n_e), protons (n_p) and negative ions (n_i), assumed known from the previous step *k*-1.

Particle orbits are determined by solving a set of *N* equations of motion:

$$m_i \frac{d\mathbf{v}_i^{(k)}}{dt} = q_i\left(\mathbf{E}^{(k-1)} + \mathbf{v}_i^{(k)} \times \mathbf{B}\right) \ , \quad i = 1,\ldots,N \qquad (2)$$

for each of the *N* particles composing the plasma. The magnetic field **B** is generated by magnets located in the source and, partially, by the currents inside the sources. An order-of-magnitude estimate shows that the latter contribution is not relevant when external fields are several tens Gauss of larger (more details are provided in Appendix A). Hence, in the following, only **B** produced by magnets will be considered. The electric field $\mathbf{E}^{(k-1)} = -\nabla\varphi^{(k-1)}$ comes from the Poisson equation (1). The charge density is proportional to the average time spent by the *N* test particles into each cell of the numerical grid spanning the whole extraction region. The right normalization constant, in physical units, is then obtained by imposing that, well inside the plasma, the density be equal to the (pre-assigned) plasma density n_p. Adequate convergence checks must be carried out: too small the number *N* and/or to coarse a mesh will cause unphysical fluctuations in the estimation of the plasma density, leading to divergence of the results.

Equation (1) must be supplemented by boundary conditions for φ, as well as by an initial guess for $\delta n^{(0)}$. This latter is chosen as: $\delta n^{(0)} \equiv 0$ everywhere, thus Eq. (1) reduces to Laplace equation $\nabla^2 \varphi^{(1)} = 0$ for $k = 1$. Boundary conditions used are sketched in Fig. (2). Plasma Grid is chosen as the ground: $\varphi_{PG} \equiv 0$. Extraction Grid is set to the value of the extraction potential: $\varphi_{EG} \equiv \varphi^{(ext)}$. A word about this: the true potential along the Extraction Grid is not uniform because of the presence of holes in that grid, see Fig. (1). The holes within all of the three grids are collinear. The electric field along the axis of the holes is reduced with respect to when one is over the metallic plate, far from the holes. In the Appendix B an analytical calculation is provided, yielding a general expression for the electric field. For the sake of simplicity, however, the hypothesis of a uniform field along the *x*-axis is retained, to be considered an average value.

Because of periodic conditions, the left- and right-hand boundary must fulfil $\nabla_n \varphi = 0$, where ∇_n is the normal derivative to the boundary, hence $\nabla_n \equiv \partial_x$.

The upper boundary is chosen deeply enough inside the plasma, that the externally applied electric field be completely shielded. In actual computations $\partial_y \varphi = 0$ as the boundary condition was used. The *x*-derivative, of course, is not exactly zero because of the perturbing effect over the spatial uniformity exerted by the hole. However, by increasing the distance from the Plasma Grid, i.e., choosing larger and larger L_{y2}, this lack of uniformity may be reduced as much as one wishes. Therefore, L_{y2} is set by the criterion that, along the upper boundary, φ be constant to within a small tolerance. This choice for the boundary condition implicitly sets the plasma potential: since $\nabla \varphi \to 0$ ($y \to \infty$), then $\varphi_{Plasma} \equiv \varphi(y = \infty)$. It is clear that this value is directly proportional to the extraction potential: $\varphi_{Plasma} \propto \varphi^{(ext)}$. However, in the real case, the plasma potential is to be partially determined by plasma interactions with the boundaries, too. Indeed, these latter should become negligible in the limiting of huge extraction potential, $\varphi^{(ext)} \to \infty$, and/or large hole width, $L_G \to \infty$.

One has still to provide starting conditions for Eq. (2). Electrons and protons were placed uniformly along *x* on top of the cell, $y = L_{y1} + d + L_{y2}$, with velocity *U* directed along the negative *y* direction. Negative ions, instead, are generated very close to the grid. In the future, the possibility for negative ions to travel longer distances through scattering with other particles will be implemented.

3. Numerical results

3.1 Electrostatic potential, electrons and positive ions

A first test run is shown in Fig. (3): the starting potential profile $\varphi^{(1)}$; electrons and protons trajectories within this potential; the second-iterate potential $\varphi^{(2)}$. Parameters were: core plasma density $n_p = 10^{17}$ m^{-3}, extraction potential $\varphi^{(ext)} = 10$ kV. Magnetic field is absent and no negative ions were considered. Geometric parameters are: L_{y1} = 4.5 mm , L_x = 21 mm , L_G = 14 mm , d = 2 mm . The Grid-plasma distance L_{y2} was set to L_{y2} = 40 mm, insuring a constancy of φ along the upper boundary: $\varphi_{Plasma} = 0.36\times\varphi^{(ext)}$ to within a tolerance of about 1%, and $\langle | \partial_y \varphi | \rangle \approx 5\times10^{-2} \times \varphi^{(ext)} /(L_{y1} + d + L_{y2})$, but in the figures only the first 2 cm from the grid into the plasma have been plotted. Fig. (4) features φ *versus y*, evaluated in the middle of the cell (x/d = 5). The kinetic energy of the particles was taken equal to the plasma potential at the plasma boundary. It is worth noticing that L_{y2} may be given the meaning of extraction depth: that is, the typical scale length over which the plasma goes from its core value (n_p) to edge value (about zero). This value may be estimated by direct measurements. The extraction depth, for high applied potentials (i.e., some kV) is, actually, a few centimeters [8], providing a (qualitative) confirmation to our model.

For this set of parameters, the contour plots for $\varphi^{(1)}$, $\varphi^{(2)}$ do appear almost identical.

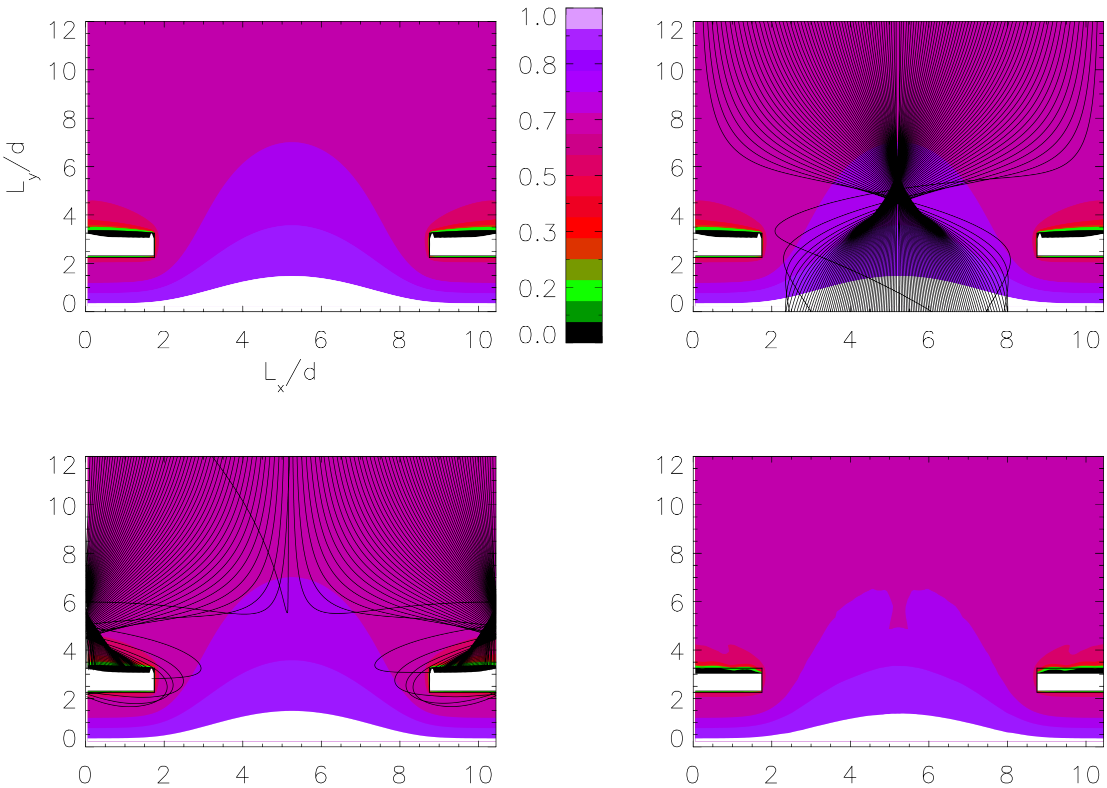

FIG. 3. Top-left: starting potential $\varphi^{(1)}$; top-right: electron trajectories; bottom-left: proton trajectories; bottom-right: first-iterate potential $\varphi^{(2)}$. Geometric, plasma and external potential parameters are given in the main text.

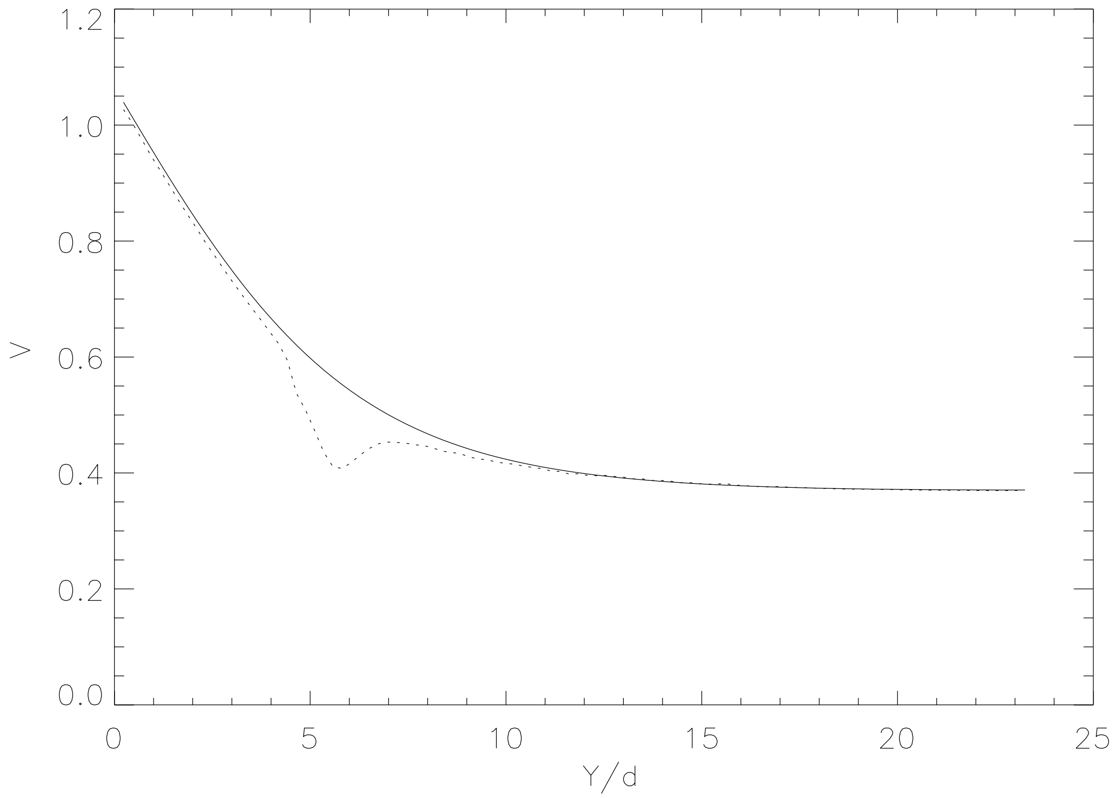

FIG. 4. Solid line, starting potential $\varphi^{(1)}$ evaluated in the middle of the cell versus *y* coordinate; dashed line, $\varphi^{(2)}$.

Eq. (1) may be made dimensionless: one may write (omitting the index *k*),

$$\begin{aligned} \tilde{\nabla}^2 \tilde{\varphi} &= -\frac{e}{\varepsilon_0} \frac{L^2 n_p}{\varphi^{(ext)}} \delta \tilde{n} \\ \tilde{\nabla}^2 &= L^2 \nabla^2, \quad \tilde{\varphi} = \varphi / \varphi^{(ext)}, \quad \tilde{n} = n / n_p \end{aligned} \tag{3}$$

where *L* is a typical size of the system. It is clear from Eq. (3) that the potential profile is dependent only upon the ratio $r = n_p/\varphi^{(ext)}$ (provided that the geometry of the source is left untouched), and not on variations for n_p, $\varphi^{(ext)}$ individually. In Fig. (3) one is exploring the case $r \approx 0$: the starting guess is expected to be the closer to the true solution, the smaller the ratio *r*. In Fig. (5) the same setup is considered, but for the extraction potential $\varphi^{(ext)}$ reduced by a tenfold factor (i.e., *r* increased by the same factor). Some differences between $\varphi^{(1)}$, $\varphi^{(2)}$ are now apparent, but on the whole it is evident that the "vacuum solution" is still a rather good estimate for the electrostatic problem. The high-$\varphi^{(2)}$ potential "triangular" region appearing in the middle of the cell (right-bottom panel) is due to the high electron charge density bunching there (see right-top panel). A scan at lower density or higher potential would yield essentially back the zero-density case of Fig. (3). The opposite scan, at higher density or lower applied potential, on the other hand, is difficult to be carried out since makes the convergence of the series (1) hard to achieve: roughly speaking, there is no guarantee of convergence once the dimensionless parameter $(e/\varepsilon_0)L^2 r$ becomes appreciably greater than unity.

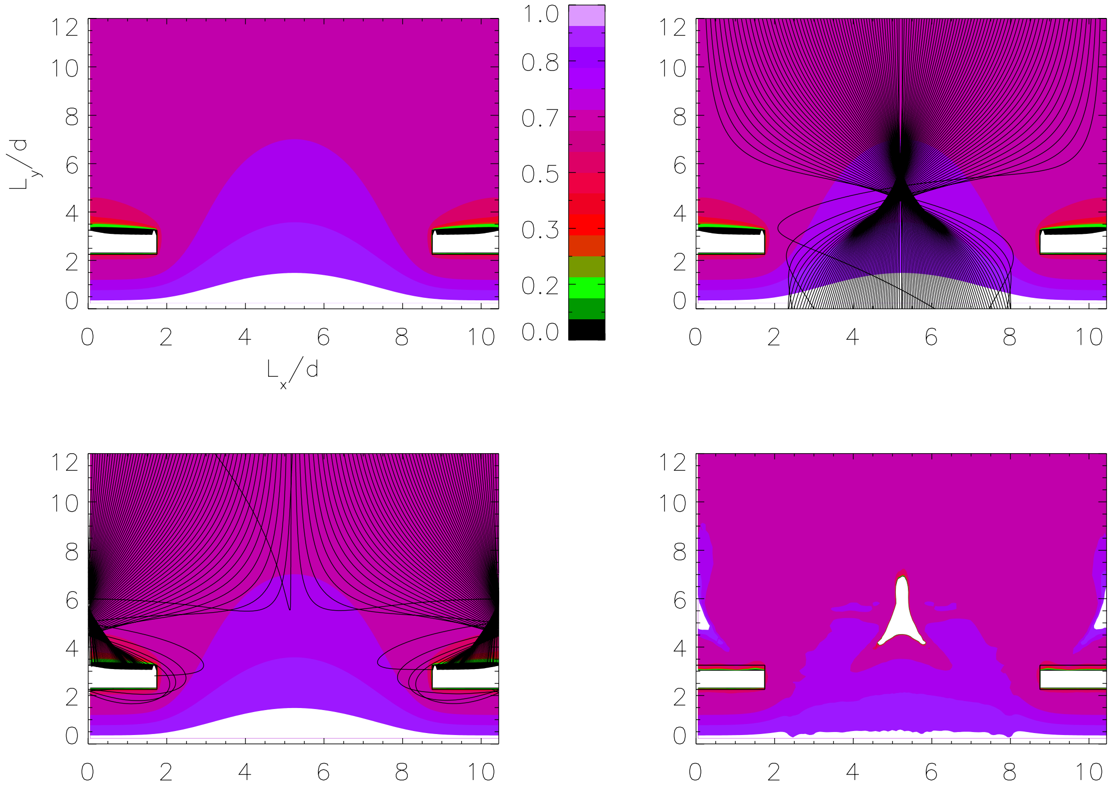

FIG. 5. Top-left: starting potential $\varphi^{(1)}$; top-right: electron trajectories; bottom-left: proton trajectories; bottom-right: first-iterate potential $\varphi^{(2)}$. Geometric, plasma and external potential parameters are given in the main text. Plasma parameters are the same as for figure 3 (see main text), but for extraction potential reduced by a tenfold factor.

3.2 Magnetic field

The magnetic filter is now added: a constant field of magnitude |B| = 50 Gauss along the *z*-axis. The presence of the magnetic field introduces a new length scale: the Larmor radius ρ_L. Figs. (6a, 6b) display electrons' trajectories for this system. The two cases differ but for the initial kinetic energy: in the former case it is chosen small, so that $\rho_L/L_{y2} < 1$; in the second case, $\rho_L/L_{y2} > 1$, i.e., electrons can reach and cross the Plasma Grid. Recall that particles are considered collisionless, hence there are not mechanisms available to shift them from their starting position more than one ρ_L along the *y* direction. A more realistic picture, including both particle-particle collisions and the thermal distribution of kinetic energy, should somewhat smear the sharp boundary out: notice, however, that a direct calculation of the mean free path for elastic Coulomb collisions shows that it is rather longer than the length scales here considered. It is apparent, in Fig. (6b), the **E**×**B** drift that moves electrons rightward (right-top panel). The results shown in Fig. (6) point to an issue that may have practical relevance. Indeed, in typical experimental conditions, the electron current accounts for about 50% (or more) of the total outgoing current [7]. It would be desirable to further reduce the electron density toward the grid, similarly to results [5], for further source optimization.

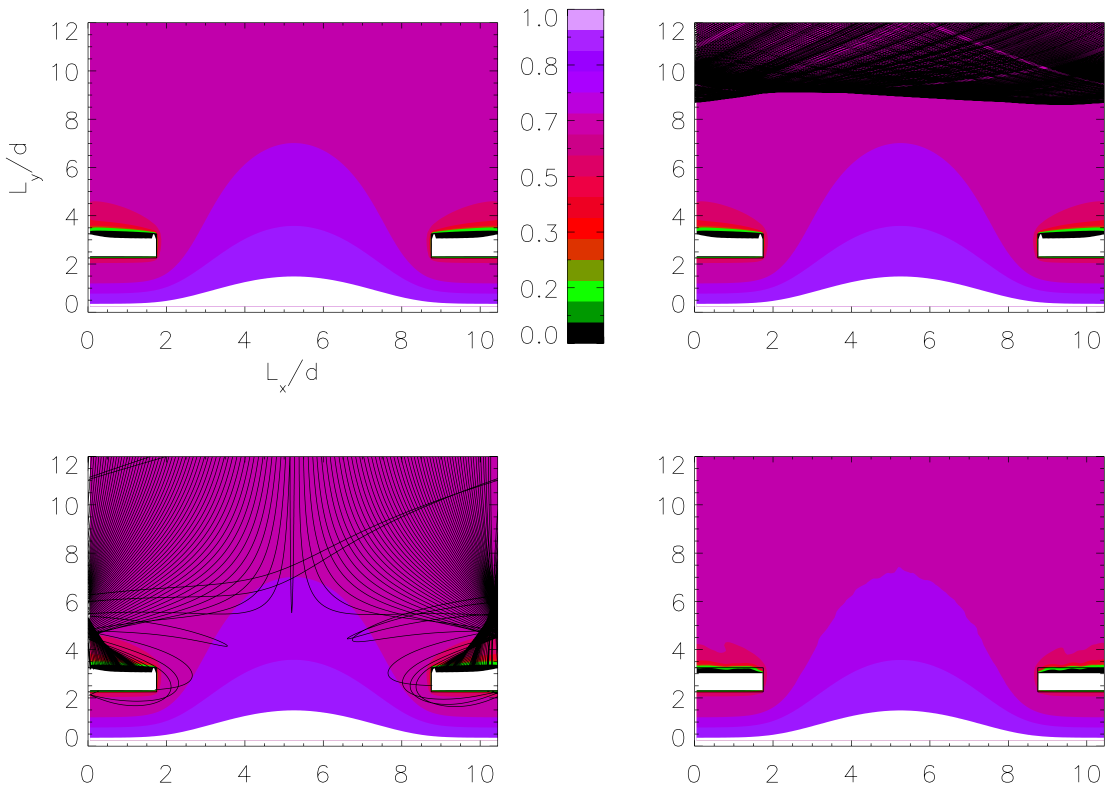

FIG. 6a. Top-left: starting potential $\varphi^{(1)}$; top-right: electron trajectories; bottom-left: proton trajectories; bottom-right: first-iterate potential $\varphi^{(2)}$. Geometric, plasma and external potential parameters are given in the main text. Magnetic field is added. Electrons are effectively shielded above y = 8.

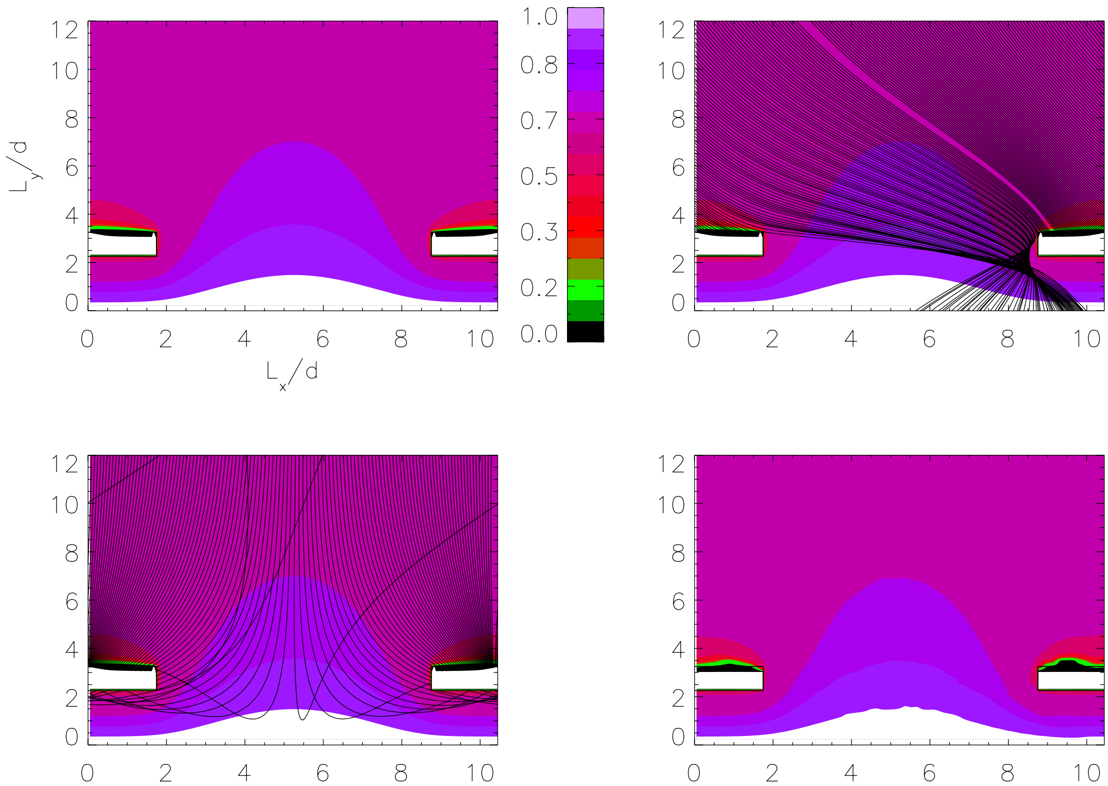

FIG. 6b. Top-left: starting potential $\varphi^{(1)}$; top-right: electron trajectories; bottom-left: proton trajectories; bottom-right: first-iterate potential $\varphi^{(2)}$. Geometric, plasma and external potential parameters are given in the main text. Magnetic field is added. With respect to Fig. (6a), initial kinetic energy of particles is increased threefold.

The effect of the magnetic filter over electron extraction efficiency was therefore studied with some detail. In Fig. (7), left panel, it is displayed the fraction f of electrons escaping the source *versus* applied magnetic field, at different kinetic energies U. For each energy there is a threshold field B_0, above which electrons are perfectly confined. It is easy to relate this field with electron energy and with initial electron location: the initial electron-grid distance L must be larger than Larmor radius ρ: $L = \rho \rightarrow B_0 \propto U^{1/2}$. The right-hand panel of Fig. (7) confirms this scaling. It may be interesting to notice that, even in the zero-magnetic-field situation, when increasing U, the fraction of escaping electrons decreases, albeit slightly. The reason is that, the greater its velocity, the lesser the electron remains sticked to electric field line. Hence, a fraction of the electrons collide with the grid even though no field line is actually intersecting it.

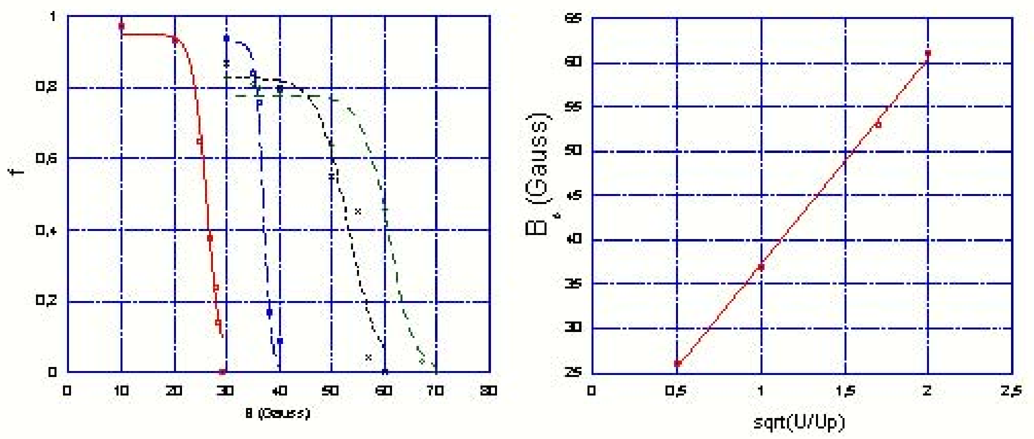

FIG. 7. Left panel: fraction *f* of electrons escaping from the source *versus* applied magnetic field. Red symbols, kinetic energy *U* is a quarter of the plasma potential, U/U_p = ¼. Blue symbols, U/U_p = 1. Black symbols, U/U_p = 3. Green symbols, U/U_p = 4. Each set of points has been interpolated with a tanh curve (solid curves), and the location of the threshold field was recovered. Right panel, threshold field *versus* electron velocity. The linear scaling is obeyed perfectly.

3.3 Negative ions

Negative ions represent eventually the main subject of this work. Fig. (8a) displays H^- trajectories under conditions that should be representative of two different generation mechanisms. In all cases, negative ions were considered to be very small in number, hence they act as test particles and do not appreciably perturb the potential profile. (It is known not to be true in all experimental situations). In one case, particles with zero kinetic energy are initialized on the surface of the Plasma Grid. This is a simplified scheme for pure surface production. In the other case, instead, particles are still initialized at a small distance from the Plasma Grid, but allowing them to be generated even in correspondence of the hole, in an attempt of simulating of volume production. The true dominating production mechanism is still a matter of debate, and is likely to be a mixture of the two, with relative weights that may change from one source to another. There is not, hence, evidence to favour one over the other. It is remarkable, however, that the present results hint that surface production should be very sensitive to geometric details of plasma grid, since only ions generated very close to the hole have some chance to escape. Of course, these figures do not take into account the relative probabilities of producing an ion on the surface or within the plasma, hence are not truly representative of the actual relative production efficiences. However, it is remarkable that, within the limitations of this code, no negative ion may be extracted provided its birth place is on the grid facing the plasma, no matter its starting velocity or extractic electric field. The reason is that, just on the grid, the electric field is such to accelerate a negatively charged particle right into the plasma. A larger initial velocity or larger electric field corresponds just to accelerating faster the particle, without altering its direction. (This statement was checked against actual simulations).On the contrary, the starting position is crucial. A first test is given by the “volume production” (Fig. 8a, left panel). Another one is provided in fig. (8b): this is still “surface production” but, here, ions are generated on the vertical face of the grid, a place where the electric field acts to extract negative particles.

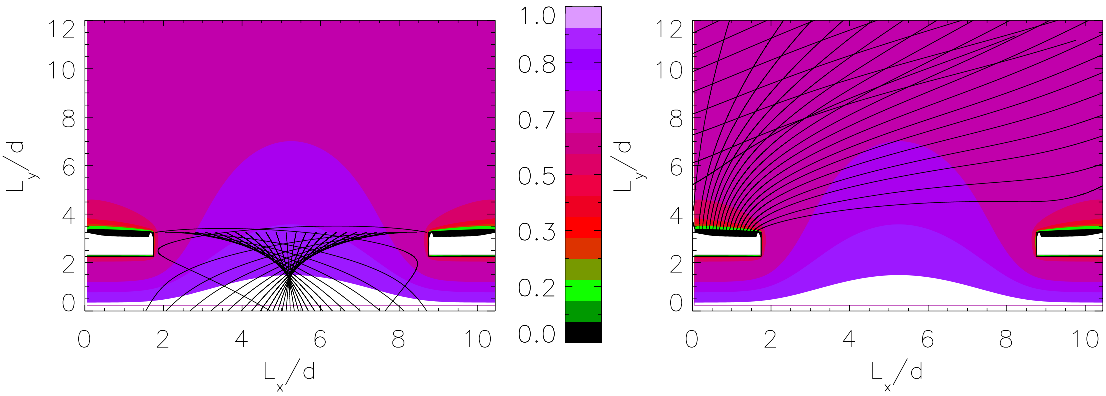

FIG. 8a. Examples of trajectories of H$^-$ ions. Left: leaving from the Grid Surface; right: produced into the plasma

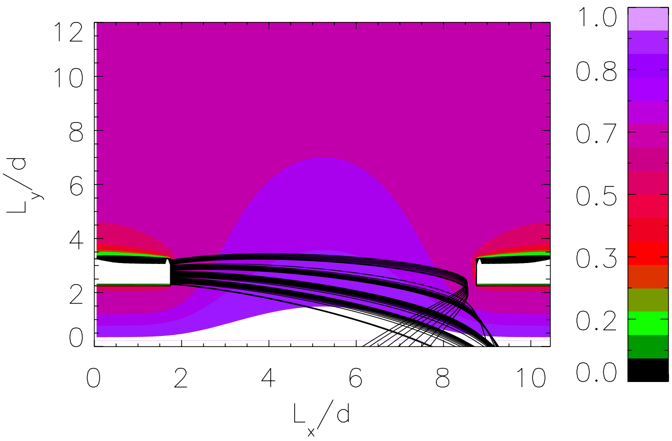

FIG. 8b. H$^-$ ions are now generated on the vertical face of the grid.

A critical issue for any consideration about actual negative ions behaviour, is their mean free path λ_{mfp}. In order for the trajectories displayed in Figs. (8) to have physical meaning, it is necessary λ_{mfp} to be order 1 cm at least. While this requirement is usually fulfilled as far as ionization/dissociation processes are involved, there is a large uncertainty related to elastic scattering through charge exchange processes, due to the large magnitude of the corresponding cross-section as well as to the large density of neutral particles.

4. Concluding remarks

The work presented in this paper is a first attempt of modelling a "realistic" high-intensity negative ion source, where the sheath theory alone is insufficient to represent the underlying physics, which is dominated by the pre-sheath region (meaning that substantial variations of potential and density take place there).

At this stage the interest was mainly in performing a sort of test of feasibility, i.e., to show that the code appears to run correctly over common situations. However, at the same time, we were able to produce some scenarios that are of interest to experimental analysis and that, to our knowledge have not yet been addressed

Appendix A

In the sheath and presheath region the charge unbalance δn and drift velocity $\mathbf{E}\times\mathbf{B}/B^2$ produce currents J which modify B. With the geometry of Fig. 2, we here assume for the sake of simplicity $\mathbf{B}$ along z and δn different from 0 in a strip $0 < y < Y$ (with $y = 0$ on the grid), where it is constant; $\mathbf{E}$ is along y (1D model).

Within the drift approximation

$$J = e\delta n \frac{E}{B} \tag{A1}$$

Ampere law gives

$$\frac{\partial B}{\partial y} = \mu_0 J \tag{A2}$$

and Gauss law is

$$\frac{\partial E}{\partial y} = \frac{e\delta n}{\varepsilon_0} \tag{A3}$$

with the boundary condition $E = 0$ at $y = Y$ (inside the plasma). In the same location, the magnetic field takes its unperturbed value $B = B_{0,}$ too. Then, putting together (A1,A2,A3), yields

$$\frac{\partial B^2}{\partial y} = 2\frac{\mu_0}{\varepsilon_0}(e\delta n)^2(y-Y) \tag{A4}$$

Solving (A4) leads to

$$\begin{aligned} &\Delta B \equiv B - B_0 = B_0\left[\sqrt{1+\Omega^2} - 1\right] \approx B_0\frac{\Omega^2}{2}, \quad \text{if } \Omega^2 < 1 \\ &\Omega^2 = \frac{\mu_0}{\varepsilon_0}\frac{(e\delta n)^2}{{B_0}^2}(y-Y)^2 \le \frac{\mu_0}{\varepsilon_0}\frac{(e\delta n)^2}{{B_0}^2}(Y)^2 \end{aligned} \tag{A5}$$

By taking B_0 = 10 Gauss, Y = 1 mm, $\delta n = 10^{16}$ m^{-3}, one finds $\Omega^2 \le 1/4$, and $\Delta B/B_0 \le$ 1/8.

Appendix B

The two grids are first supposed to be two plates without holes, extending indefinitely along x and z axes. Hence, one may model the region between the two grids as a plane capacitor. The surface charge density on the plates of such a capacitor would be $\sigma = \pm\varepsilon_0 \Delta V / L_{y1}$, with ΔV difference of potential between the two plates.

Let us now introduce holes in the Extraction Grid. For the sake of simplicity, just one hole is considered: the real multiple-holes case may be easily handled. In correspondence of the hole, surface charge density must vanish. Hence, the hole is modelled as a cylinder with radius a and with a surface charge density $\sigma_{Hole} = -\sigma_{EG}$. The potential produced by the cylinder, V_{Hole}, may be found in textbooks on electrostatics [9]:

$$\begin{aligned} &V_{Hole} = \frac{\sigma_{Hole}}{2\pi\varepsilon_0}\left[-\pi y + r_1\Im_2(k) + \frac{a^2 - R^2}{r_1}\Im_1(k) + \frac{y^2}{r_1}\frac{a-R}{a+R}\Im_3(k,m)\right], \\ &R^2 = x^2 + z^2, \quad r_1 = \sqrt{(a+R)^2 + y^2}, \quad k = \frac{2\sqrt{aR}}{r_1}, \quad m = \frac{2\sqrt{aR}}{(a+R)}, \\ &\Im_1(k) = \int_0^{\pi/2}\frac{d\psi}{\sqrt{1-k^2\sin^2\psi}}, \quad \Im_2(k) = \int_0^{\pi/2} d\psi\sqrt{1-k^2\sin^2\psi}, \\ &\Im_3(k,m) = \int_0^{\pi/2}\frac{d\psi}{\sqrt{1-k^2\sin^2\psi}\left(1-m^2\sin^2\psi\right)} \end{aligned} \tag{B1}$$

where $y = 0$ at the Extraction Grid, and $E_A = \Delta V/L_{y1}$.

This expression is greatly simplified for R = 0, i.e., along the axis of the hole, that is the region one is most interested in:

$$R=0\rightarrow k,m=0\rightarrow \Im_1=\Im_2=\Im_3=\pi/2,\ r_1^2=a^2+y^2$$

$$V_{Hole}=\frac{\sigma_{Hole}}{2\pi\varepsilon_0}\left[-\pi y+\pi r_1\right]=\frac{E_A}{2}\left[-y+\sqrt{a^2+y^2}\right] \tag{B2}$$

$$\rightarrow E_{Hole,x}(R=0)\equiv-\frac{dV_{Hole}}{dy}=\frac{E_A}{2}\left[1-\frac{y}{\sqrt{a^2+y^2}}\right]$$

This field must be subtracted off from the capacitor field.

Ackowledgments

The result in the appendix B was brought to authors' attention by Nicola Vianello.

References

[1] Whealton J H, Olsen D K, and Raridon R J 1998 *Rev. Sci. Intrum.* **69** 1103

[2] Peters J 2002 *Rev. Sci. Instrum.* **73** 900

[3] Welton R F, *et al* 2002 *Rev. Sci. Instrum.* **73** 1013

[4] Becker R 2004 *Rev. Sci. Instrum.* **75** 1687; *ibid*, 1723.

[5] Sakurabayashi T, Hatayama A, Bacal M 2004 *J. Appl. Phys.* **95** 3937

[6] Bandyopadhyay M, *et al* 2004 *J. Appl. Phys.* **96** 4107

[7] Franzen P, talk held at RF Source Technical Meeting (Garching, 25-26th January 2005). Unpublished.

[8] Tanga A 2004 private communication

[9] Durand E 1964 *Electrostatique* (Masson et C.ie Editors, Paris, vol. I, p. 250 – in French)